

# r.avaflow v4, a multi-purpose landslide simulation framework

Martin Mergili<sup>1</sup>, Hanna Pfeffer<sup>1</sup>, Andreas Kellerer-Pirklbauer<sup>1</sup>, Christian Zangerl<sup>2</sup>, Shiva P. Pudasaini<sup>3,4</sup>

<sup>1</sup>Cascade – Mountain Processes and Mountain Hazards, Department of Geography and Regional Science, University of Graz, Heinrichstraße 36, 8010 Graz, Austria

5 <sup>2</sup>Institute of Applied Geology, University of Natural Resources and Life Sciences (BOKU), Peter-Jordan-Straße 82, 1190 Vienna, Austria

<sup>3</sup>School of Engineering and Design, Chair of Landslide Research, Technical University of Munich, Arcisstraße 21, 80333 Munich, Germany

<sup>4</sup>Kathmandu Institute of Complex Flows, Kageshwori Manohara–3, Bhadrabas, Kathmandu, Nepal

10 *Correspondence to:* M. Mergili (martin.mergili@uni-graz.at)

**Abstract.** We present r.avaflow v4, an enhanced version of the open-source mass flow simulation tool r.avaflow. The updated version includes, among other new functionalities, (i) a layered model, where the individual phases move on top of each other instead of mixing; (ii) a mechanically controlled landslide deformation model, supporting the entire range from block sliding to full deformation; (iii) a slow-flow model, allowing for the simulation of landslides beyond extremely rapid  
15 processes, using an equilibrium-of-motion model; and (iv) an interface for 3D and virtual reality visualization of the results. We use four case studies to demonstrate the functionalities introduced to r.avaflow v4 and to discuss the related chances and challenges: (i) a generic planar rock slide with interlayer shearing, and (ii)–(iv) semi-generic representations of the prehistoric Köffels rock slide (Austria), the prehistoric East Fogo landslide and tsunami (Cape Verde), and the Dösen rock glacier (Austria). Our results clearly reveal the high potential of the additional functionalities to widen the scope of r.avaflow  
20 beyond the simulation of extremely rapid and freely deforming mass flows. Combinations of the layered model, mechanically controlled deformation, and the slow-flow model unlock potentials yet barely explored in the field of GIS-based landslide simulations. In addition, the layered model facilitates a more realistic simulation of landslide-reservoir interactions. We also highlight the limitations regarding the physical basis and the application of the functionalities presented. Our enhancements are particularly useful for improved process visualization targeting at awareness building and  
25 environmental education. They are also suitable to be used for scenario-based predictive simulations in combination with a thorough empirical evaluation campaign.

## 1 Introduction

Mass flow simulation tools are used for numerically reconstructing, predicting, and communicating flow-type landslide processes. The first conceptual model for mass flows dates from the 1930s (Heim, 1932), and the first physically-based  
30 approach from the 1950s (Voellmy, 1955). More sophisticated models have evolved from the earlier models over time. By the mid-2020s, many practitioners still prefer physically rather simple models put into user-friendly interfaces, such as the

RAMMS software (Christen et al., 2010). At the same time, scientific attention is paid to two-and multi-phase models such as OpenLISEM, integrating slope hydraulics, landslide release, landslide, and landslide runout (Bout et al., 2021) or r.avaflow, a flexible multi-phase computational framework focused on complex, cascading landslide processes, and on a full 3D implementation of the material point method (Cicoira et al., 2022).

We focus on r.avaflow, a Geographic Information System (GIS) based open-source simulation framework for mass flows and related process chains. It was first introduced by Mergili et al. (2017), at that time based on the two-phase mass flow model of Pudasaini (2012), with a solid and a fluid phase. The tool was then continuously extended and equipped with a third, fine-solid, phase (Pudasaini and Mergili, 2019). It was applied to a number of case studies, mainly regarding geomorphic process chains in high-mountain environments, such as the 2012 Santa Cruz glacial lake outburst flood (GLOF) (Mergili et al., 2018a), the complex landslides in 1962 and 1970 at Huascarán (Mergili et al., 2018b), the 2017 Piz Cengalo-Bondo process chain (Mergili et al., 2020a), the 1941 Palcacocha GLOF (Mergili et al., 2020b), the 2020 Salkantay GLOF (Vilca et al., 2021), the 2020 Jinwuco GLOF (Zheng et al., 2021), the 2021 Chamoli process chain (Shugar et al., 2021), and, most recently, the 2023 South Lhonak GLOF process chain (Sattar et al., 2025).

The various case studies have highlighted the potentials of the r.avaflow software, but also revealed remaining limitations and need for enhancement, which can be summarized as follows:

- (1) Forward simulations remain a particular challenge, especially for complex process chains, since parameters must be calibrated with observed and documented mass flow characteristics. Guiding parameter sets for future simulations would have to rely on a large number of back-calculations of documented events (Mergili et al., 2018b).
- (2) r.avaflow is only suitable for extremely rapid processes. It was not designed for slower processes dominated by viscosity. A prototype of a slow-flow model was nevertheless implemented recently (Su et al., 2024; Section 2.4).
- (3) r.avaflow is designed for more or less freely deforming flow-type processes. It is unsuitable for slide-type movements with limited deformation. However, a prototype for deformation control (Pudasaini and Mergili, 2024a) was included recently.
- (4) Each of the phases is clearly associated with a particular rheology, without a lot of flexibility (e.g., the solid, fine-solid and fluid phase in Pudasaini and Mergili, 2019). A Voellmy-type rheology (Voellmy, 1955) is only available with the single-phase model.
- (5) Even though the tool is able to cope with three phases, there is always a mixture of the phases assumed. E.g., the behaviour of a landslide moving and depositing at the bottom of a reservoir without substantial mixing with the water cannot be simulated. Preliminary computational experiments with large-scale volcanic flank collapses have revealed a strong need to revisit and to enhance the concepts of r.avaflow in regard to the simulation of landslide-to-reservoir impacts.
- (6) The user interface basically consists in a start script which has to be written manually, without a capable user interface. The software is tightly coupled with the Geographic Information System GRASS GIS (GRASS Development Team, 2025) and bound to UNIX systems.

(7) Raster maps, text files and map and animation plots are provided as output, but there are no direct interfaces to more advanced visualization systems.

We do not consider challenge (1) in this work. The issue of guiding parameter sets and forward simulations has to be the subject of further investigations, e.g., by applying machine learning and artificial intelligence methods (Yildiz et al., 2023).  
70 Instead, we focus on the challenges (2)–(7), along with some other aspects, to enhance the scope and usability of the `r.avafLOW` mass flow simulation framework. We note that for (2), (3), and (5), we are not aware of any comparable software tools appropriately dealing with the challenges mentioned. In Section 2, we will introduce `r.avafLOW` v4 and its new functionalities, compared to the older versions. Furthermore, in Section 3 and Section 4 we will demonstrate the functionalities using a set of generic and semi-generic case studies. We will discuss our findings in Section 5 and conclude in  
75 Section 6.

## 2 The simulation framework `r.avafLOW`

### 2.1 General concept of `r.avafLOW`

`r.avafLOW` is a GIS-based open-source mass flow simulation framework. The model applies physically-based equations to numerically estimate and calculate the motion of mass and momentum of up to three phases through a regular grid. The two-  
80 phase model of Pudasaini (2012) was employed in the original version (Mergili et al., 2017). It was later upgraded by the three-phase model of Pudasaini and Mergili (2019), with a solid, a fine-solid, and a fluid phase, each associated with pre-defined rheologies: the solid phase is characterized through internal and basal friction, the fine-solid phase additionally through viscosity and yield strength, and the fluid phase through viscosity and yield strength. Interactions between the phases are considered through buoyancy effects, virtual mass, and drag. A Voellmy-type mixture model is available as an  
85 alternative. The mass and momentum balance equations in Pudasaini and Mergili (2019) are depth-averaged, and the phases are considered to be mixed over the flow height, even though the vertical distribution of the concentration of the individual phases can be controlled. A TVD-NOC (Total Variation Diminishing Non-Oscillatory Central Differencing) scheme on a staggered grid is used for mass and momentum transport (Tai et al., 2002). We use the scheme in the way described by Wang et al. (2004).  
90 Typically, the release mass is defined through raster maps showing the release heights for each cell and each phase, imposed on a digital terrain model. Hydrographs defined by discharge, and flow velocities are provided at those locations (not only for water, but for all types of materials considered in `r.avafLOW`) and can also be used for the input mass and momentum to the system. Additional functionalities include entrainment, stopping, non-hydrostatic dispersive motion, spatio-temporal variation of several parameters and controls, and empirical evaluation of the results. The readers are directed to the `r.avafLOW` web site (Mergili and Pudasaini, 2025) for further information. The output of `r.avafLOW` essentially consists in time series of  
95 ascii raster maps and plots of flow height and (optionally) kinetic energy and dynamic pressure, along with text files summarizing the simulation.

## 2.2 New features of r.avaflow v4

In contrast to earlier versions of r.avaflow, with pre-defined solid, fine-solid, and fluid phases (Pudasaini, 2012; Mergili et al., 2017; Pudasaini and Mergili, 2019), there is no a-priori distinction between different rheologies in r.avaflow v4: rheologies are automatically determined, depending on the user input. For the sole purpose of representation, we provide a quick and informal overview of the multi-phase momentum balance equation:

$$W_t + F_x + G_y = \alpha h H(GA, DR, EC, FE, TF, FF, AD, VT) \quad (1)$$

For the rigorous, formal descriptions of the model equations, we refer to Pudasaini and Mergili (2019) and the other relevant references mentioned above and in Table 1. Eq. (1) applies to the x and y directions for each of the (minimum 1, maximum 3) phases. The flux terms  $W_t$ ,  $F_x$ , and  $G_y$  are expressed as the time derivatives of the state variables, and the momentum and the momentum flux derivatives in x and y direction.  $\alpha$  is the volumetric fraction of the relevant phase, and  $h$  is the total flow height.  $H$  is a function of all the applied forces: the gravitational acceleration ( $GA$ ), internal deformation ( $DF$ ), drag ( $DR$ ), an extended Coulomb term ( $EC$ ), fragmentation and energy loss through shearing ( $FE$ ), turbulent friction term ( $TF$ ), fluid friction term ( $FF$ ), ambient drag term ( $AD$ ), and the viscous stress terms ( $VT$ ). We note that  $EC$ ,  $EL$ ,  $TF$ ,  $FF$ ,  $AD$ , and  $VT$  can only decelerate motion. This implies that, in sum, these terms do not induce a change in the direction of motion. From a purely mathematical point of view, the flow at the given raster cell would stop if such a change of direction would occur. All terms are elaborated in more detail in Table 1. All key parameters used in the equations of Table 1 can be defined as global values or as raster maps, where individual values can be provided for each raster cell. Detailed information on all aspects exceeds the scope of this work and is provided in the referenced publications in Table 1.

The behaviour of the landslide depends on the definition of the parameters associated to each term. All terms can be deactivated by setting the governing input parameters to zero. Where necessary, it is automatically decided whether to consider a material as solid or as fluid: solid material is assumed if the internal friction angle  $\varphi > 0$ . Otherwise, the material is considered fluid. Buoyancy is only considered with respect to fluid phases of lower density. Not all combinations of terms are necessarily physically meaningful, so that the enhanced flexibility for users also implies an increased responsibility to combine terms in a meaningful way.

**Table 1: x-directional flux and source terms governing flow dynamics in r.avaflow v4, for any of the maximum of three phases. Terms in y direction are formulated in an analogous way.  $u_x$  and  $u_y$  = depth-averaged velocities in x and y direction;  $uu_{vm}$  and  $uv_{vm}$  = virtual mass contributions (Pudasaini and Mergili, 2019);  $DT$  = dispersion term (Pudasaini, 2023);  $g_x^*$  = effective downslope component of gravity in x direction;  $f_{dx}$  = deformation coefficient in x direction (Pudasaini and Mergili, 2024a);  $k_x$  = x-directional earth pressure coefficient;  $g_x^+$  and  $g_z^+$  = effective slope-normal components of gravity, including the different buoyancy effects (Pudasaini and Mergili, 2019);  $g_z^*$  = effective slope-normal components of gravity, including buoyancy and curvature effects;  $c_{DRAG}$  = drag coefficient (Pudasaini and Mergili, 2019), corrected for the relevant buoyancy effects;  $\Delta u_x$  = velocity difference in x direction with respect to another phase;  $\Delta|u|$  = difference in absolute velocities with respect to another phase;  $\delta$  = basal friction angle;  $c$  = cohesion;  $E_v$  = energy loss through shearing coefficient (Pudasaini and Mergili, 2024b);  $\varphi$  = internal friction angle;  $F_{ml}$  = fragmentation number (Pudasaini et al., 2024);  $\zeta$  = turbulent friction number;  $n$  = Manning number, accounting for the roughness of the basal surface for the fluid phase;  $c_{AD}$  = ambient drag coefficient, and  $\tau$  = viscous stress. Bold letters denote input parameters.**

Term	Equation	Remarks
Time derivative of the state variables	$W_t = \frac{\partial}{\partial t}(\alpha h)$	
Momentum flux derivative in x direction	$F_x = \frac{\partial}{\partial x} \left[ \alpha h \left( u_x^2 + \beta_x \frac{h}{2} \mp uu_{vm} \right) + DT \right]$	
Momentum flux derivative in y direction	$F_y = \frac{\partial}{\partial y} [\alpha h (u_x u_y \mp uv_{vm})]$	
Gravitational acceleration	$SL = g_x^*$	Global component included with enhanced deformation control (Section 2.4)
Internal deformation (solid)	$DF = -f_{dx} k_x g_z^+ \cdot \frac{\partial h}{\partial x} - g_z^- \frac{\partial h}{\partial x}$	Buoyancy effects in square brackets
Internal deformation (fluid)	$DF = -g_z^+ \cdot \frac{\partial h}{\partial x}$	
Drag	$DR = \pm \frac{1}{\alpha} c_{DRAG} \Delta u_x  \Delta u ^{j-1}$	One drag term with respect to each other phase, if fluid; see Pudasaini and Mergili (2019) for details; not valid for layered model (Section 2.3)
Extended Coulomb term	$EC = \frac{u_x}{ u } \tan \delta g_z^* + \frac{c}{\alpha h}$	
Fragmentation and energy loss through shearing	$F_{ml} u_x \pm E_{sp} \tan \varphi E_v \frac{\partial u_x}{\partial x} \frac{\partial h}{\partial x}$	See Table 2 for explanation and references
Turbulent friction	$TF = \frac{u_x  u }{\alpha h \zeta}$	Voellmy-type model: Coulomb term and turbulent friction
Fluid friction	$FF = \frac{n^2}{h^{4/3}} u_x  u $	Simplified application of the Manning equation

Ambient drag	$AD = c_{AD} u_x  u $	Can be used to account for fluid/air resistance
Viscous stress	$VT = \nabla \cdot (\alpha \tau)$	See Pudasaini and Mergili (2019)

135

The Voellmy-type model is available for each phase, by combining the Coulomb term with the turbulent friction term. Apart from rethinking the general concept of the phases, some additional functionalities have been introduced (some of them as prototypes already in the previous version r.avaflow v3). They are summarized in Table 2.

140

**Table 2: Additional functionalities available in r.avaflow v4. Those functionalities considered in detail in this study are written in bold letters.**

Functionality	Description	References
<b>Layer model</b>	The phases are arranged on top of each other, instead of mixed together.	
<b>Deformation control</b>	Internal deformation of the moving mass is mechanically controlled, based on material strength or resistance, allowing to simulate the whole range between free flow and block sliding.	Pudasaini and Mergili (2024a)
<b>Slow-flow model</b>	An equilibrium-of-motion model is employed to simulate the motion of viscosity-dominated flows which are not extremely rapid.	Su et al. (2024)
Fragmentation model	Fragmentation processes in rock avalanches can be included.	Pudasaini et al. (2024)
Energy loss through shearing model	Energy loss through shearing can be considered in the simulation.	Pudasaini and Mergili (2024b)
Dispersion model	Dispersion processes can be included in the simulation.	Pudasaini (2023)
<b>Virtual reality interface</b>	csv files and Python scripts facilitate the integration of the simulation results in 3D and VR visualization tools.	
Web-based user interface	Manual, data and parameter input, and generation of start scripts and parameter files are enabled through a Web interface.	Mergili and Pudasaini (2025)

The models for fragmentation (Pudasaini et al., 2024), energy loss through shearing (Pudasaini and Mergili, 2024b), and dispersion (Pudasaini, 2023), which have been introduced earlier, will not be further discussed here. The model for deformation control has been introduced by Pudasaini and Mergili (2024a), but an enhanced version is used in the case studies introduced in Section 3. We now introduce the layered model, the enhanced deformation control, the slow-flow model, and the virtual reality interface. We point out that all these models can be combined with each other (Section 3 and Section 4).

## 2.3 Layered model

When a landslide hits a reservoir, simulation with a depth-averaged multi-phase mixture model results in a mixture of solid landslide material and fluid water. The solid and fluid column of material is not resolved, and the phases are mixed along the vertical or slope-normal profile of the flow mass. For example, for a two-phase model involving a frictional solid phase, this means that the entire column of material is effectively frictional. The way the pressure gradients are computed will prevent the fluid phase from behaving independently from the solid phase. In situations where the solid fraction is significant, the original water surface might not recover, depending on the specific situation and model parameterization. Such a behaviour is not realistic in those cases where a landslide deposits at the bottom of a reservoir. This phenomenon is particularly obvious in the results of simulations where large landslides deposit at the bottom of deep reservoirs, whereas it is less clearly visible where small landslides interact with rather shallow water bodies.

In many real-world-cases, however, we can assume such a solid-dominated bottom and a fluid-dominated top, connected by a mixture layer. In the present work, we simplify this pattern to a maximum of three layers, with phase 1 at the bottom, an optional phase 2 in the middle, and phase 3 at the top, i.e., the individual phases are arranged on top of each other instead of mixed together (Fig. 1a). Thereby, each layer represents one phase, meaning that individual layers cannot be multi-phase. To achieve this, we control the gravity components, the flow height gradients, and the drag forces:

- Gravity components  $g_x^*$ ,  $g_y^*$ ,  $g_z^*$ ,  $g_z^+$ , and  $g_z^-$ : with the layered model, the gravity components for phase 2 and phase 3 are not computed from the slope of the basal surface, but from the slope of the upper surface of the layer below. This means that the upper surface of phase 1 is considered the basal surface of phase 2, and the upper surface of phase 2 is considered the basal surface of phase 3. Buoyancy effects on the gravity components are not considered for the layered model.
- Flow height gradients  $\partial h / \partial x$  and  $\partial h / \partial y$ : in the standard mixture model introduced in Section 2.1, the effective flow height for internal deformation is the total mixture height  $h_e = h$ . In the layered model each phase P1–P3 has its own effective material height,  $h_e = h_{P1}$  for phase 1,  $h_e = h_{P2}$  for phase 2, and  $h_e = h_{P3}$  for phase 3. This ensures that each phase deforms individually, but with the effect of the evolving geometry of the underlying phase.
- Drag  $DR$ : with the standard model, the drag is computed according to Pudasaini and Mergili (2019) for each phase in the mixture. This concept, however, is not applicable to layered movements, for which we introduce the following approximation for the drag coefficient in x direction  $C_{Dx}$ :

$$\text{if } \text{sgn} \frac{\partial h_{P1}}{\partial x} = \text{sgn} (u_{x,P2} - u_{x,P1}) \text{ and } |u_{x,P1}| > |u_{x,P2}|: C_{Dx} = f_{DR} \cdot \sin \left( \arctan \frac{\partial h_{P1}}{\partial x} \right) \cdot \alpha_{P1}, \quad (2)$$

where P2 is a fluid phase moving on top of a solid phase P1.  $f_{DR}$  is a scaling factor. The drag coefficient in y direction  $C_{Dy}$  is computed in an analogous way. If the condition given in Eq. (2) is not met,  $C_{Dx}$  is set to 0. Note that P1 and P2 are only used as an example. The same principle applies to combinations of P1 and P3 or P2 and P3. The ideas behind this concept are that (i) drag only acts if the thickness gradient of the solid phase goes into the same direction as the relative velocity difference between the fluid and the solid phase; (ii) drag only acts when the solid moves faster than the fluid; and (iii) the drag coefficient is proportional to the sine of the gradient of solid flow height (i.e., there would be no drag if the surface of the solid part of the flow would run parallel to the terrain slope and, theoretically, the drag coefficient would be 1 in the case of a vertical wall and  $f_{DR} = 1$ ). Fig. 1b illustrates some selected examples of drag coefficients (assuming  $f_{DR} = 1$ ) computed with this approach.

We note that the layered model is not only useful for landslide-reservoir interactions, but also for layered landslides (Section 3 and Section 4).

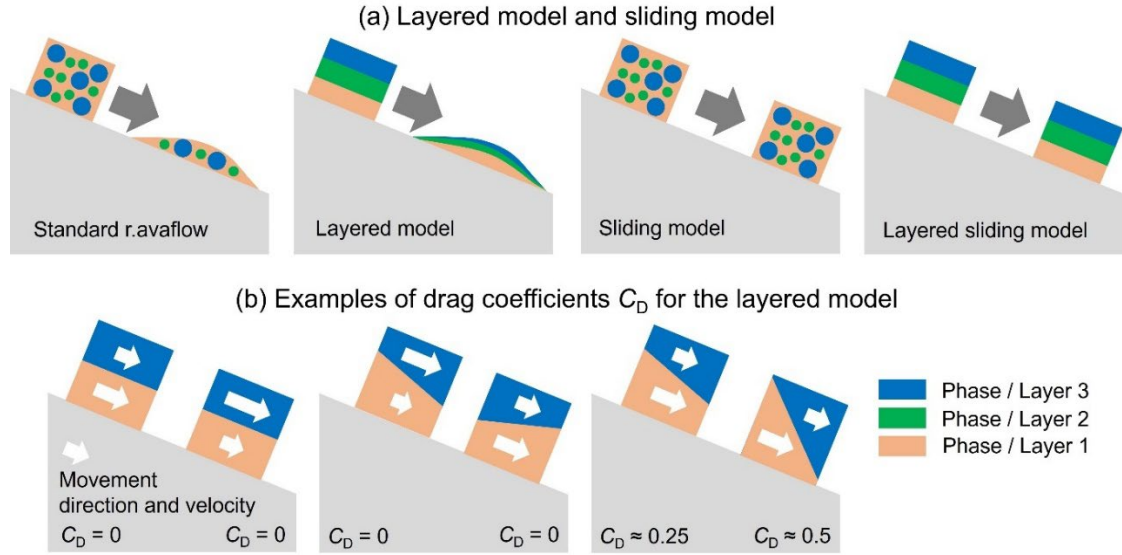


**Fig. 1:** Schematic sketch illustrating the effects of the new model components of r.avaflow v4, using profiles along the down-slope direction. (a) Comparison of the standard model used in r.avaflow, with maximum 3 phases (Pudasaini and Mergili, 2019); the layered model, where the phases are not mixed, but arranged on top of another; the model with deformation control, where the deformation of the moving mass is controlled; and the combination of the layered model and the deformation control. (b) Examples of drag coefficients computed with the layered model (examples here with two distinct layers) for selected idealized situations.

## 2.4 Enhanced deformation control

We use the controlled deformation model introduced by Pudasaini and Mergili (2024a). This model can be applied to all phases with internal friction angle  $\varphi > 0$  and builds on the effective deformation factors  $f_{dx}$  in x direction and  $f_{dy}$  in y



direction, both in the range 0–1, where  $f_{dx}, f_{dy} = 0$  completely locks the deformation (as shown in Fig. 1a), and  $f_{dx}, f_{dy} = 1$  allows full deformation (identical to the model without deformation control).  $f_{dx}$  and  $f_{dy}$  are no input parameters. The input value is the raw deformation factor  $f_d^*$ , which is enhanced with the earth pressure coefficient  $K$  and the gravity components in z direction  $g_{zx}$  or  $g_{zy}$ , respectively:

$$f_{dx} = 1 - \frac{(1-f_d^*)g_z^*}{Kg_{zx}}, f_{dy} = 1 - \frac{(1-f_d^*)g_z^*}{Kg_{zy}}, \quad (3)$$

where  $g_z^*$  is the gravity component in z direction at the steepest raster cell of the release area.

In cases where landslides move as one rigid block, it might be reasonable to assume that the motion of the entire block is governed by global values of the gravity components, applied to each raster cell instead of the local gravity components depending on the local slope components. For this purpose, the global gravity components  $g_x^g$ ,  $g_y^g$ , and  $g_z^g$  are introduced, representing the mean values of the local gravity components  $g_x$ ,  $g_y$ , and  $g_z$  over the entire sliding mass, weighted for flow height and updated at each time step of the simulation. Global gravity components are optionally applied in the gravitational acceleration term ( $g_x = g_x^g$ ,  $g_y = g_y^g$ ) and the deceleration term ( $g_z = g_z^g$ ) for frictional material. For simplicity this is referred to as global sliding, whereas the conventional way to consider each raster cell individually is referred to as local sliding. Global and local sliding can also be combined, with the parameter  $f_g$  denoting the fraction of global sliding.

## 2.5 Slow-flow model

Hungr et al. (2014) describe all landslides moving at  $>5$  m s<sup>-1</sup> as extremely rapid. This velocity class roughly defines the scope of the momentum balance model used in r.avaflow. To extend the applicability to slower landslides, an equilibrium-of-motion model has been adopted. This method, outlined by Su et al. (2024), is founded on the premise of a viscous downslope mass flow, with the flexibility to include a viscous base layer of minor thickness. It represents a simple and intuitive approach, at the cost of neglecting or simplifying some aspects, such as the evolution of pore water pressure.

Assuming a planar Couette flow, the viscous forces in x and y direction are counterbalancing the gravitational force, which substitutes the forces exerted by the upper surface. Regarding the properties of individual cells, the mass is proportional to the landslide height  $h$ , while the landslide density  $\rho$  and the surface area  $A$  are normalized:

$$F_L = \mu A \frac{u}{h} \rightarrow ahAp = \nu \rho A \frac{u}{h} \rightarrow g_x h = \nu \frac{u_{xe}}{h}, g_y h = \nu \frac{u_{ye}}{h} \rightarrow u_{xe} = \frac{g_x h^2}{\nu}, u_{ye} = \frac{g_y h^2}{\nu}, \quad (4)$$

where  $F_L$  is the force acting on the landslide mass,  $\mu$  and  $\nu$  are the dynamic and kinematic viscosities,  $u$  is the flow velocity at the upper surface of the landslide,  $a$  is the acceleration of the landslide, and  $g_x$  and  $g_y$  are the downslope gravity components in x and y direction.  $u_{xe}$  and  $u_{ye}$  are the equilibrium velocities in x and y directions.

Multiplying  $u$  and  $\nu$  by  $h$ , yields the normalized momenta  $p_x$  and  $p_y$ . Thus, the velocities of the deforming mass ( $u_x$  in x direction and  $u_y$  in y direction) decrease linearly along the vertical profile from top to bottom (base velocities  $u_{xb}$ ,  $u_{yb}$ ).

Accordingly,  $u_x$  and  $u_y$  represent the mean velocities within the landslide column of the depth-averaged model, while the surface velocities of the landslide are  $[2(u_x - u_{xb})] + u_{xb}$  and  $[2(u_y - u_{yb})] + u_{yb}$ . The first terms of Eq. (5) thus describe the deformation of the landslide and the second terms represent the basal movement.

$$p_x = h \left( \frac{g_{xt} h^2}{2\nu} + \frac{g_{xb}^*}{\xi} \right), p_y = h \left( \frac{g_{yt} h^2}{2\nu} + \frac{g_{yb}^*}{\xi} \right), \quad (5)$$

where  $g_{xt}$  and  $g_{yt}$  are the downslope components of gravity in x and y direction at the top of the landslide (i.e., including gradients of flow height),  $\nu$  is the kinematic viscosity of the mass,  $g_{xb}^*$  and  $g_{yb}^*$  are the downslope components of the effective gravity (Section 2.3) in x and y direction at the bottom of the landslide. The ratio between the kinematic viscosity and the square of the basal layer thickness is represented by  $\xi$ .

Mass and momentum fluxes between cells follow the conventions of traditional flow models (Savage and Hutter, 1989; fluid terms in Pudasaini, 2012; Pudasaini and Mergili, 2019). Calculating momenta from Eq. (5) results in their evolution in equilibrium with accelerating and decelerating forces at the individual grid cells. Hence, those momenta cannot act as source of momentum production or dissipation. Compared to momentum balance models one major advantage is the simple approach to time-scaling. Time-scaling can be directly applied to  $u$  and  $v$ , without the necessity to adjust any additional variables. It is important to emphasize that the outlined method neglects inertial effects and consequently must not be applied for the simulation of extremely rapid mass flows (according to the definitions of Hungr et al., 2014).

## 2.6 Virtual reality interface

r.avafLOW v4 includes an interface for 3D and virtual reality (VR) visualization of the model results. For this purpose, a time series of csv files – one for each output time step, based on a fixed interval defined by the user – is automatically produced, describing the geometric information (elevation of the landslide surface and, optionally, elevation of the terrain surface and individual layers) for each raster cell along with red, green, and blue (RGB) colour values to be used for visualization. The RGB values are composed of the following pieces of information, which can be combined in different ways:

- landslide heights and composition of phases (updated for each time step);
- shaded relief information (updated for each time step);
- and orthophoto information, if an orthophoto is provided by the user. Optionally, the raster cell values of the orthophoto can be shifted to follow the motion of the landslide, allowing for a more realistic visualization.

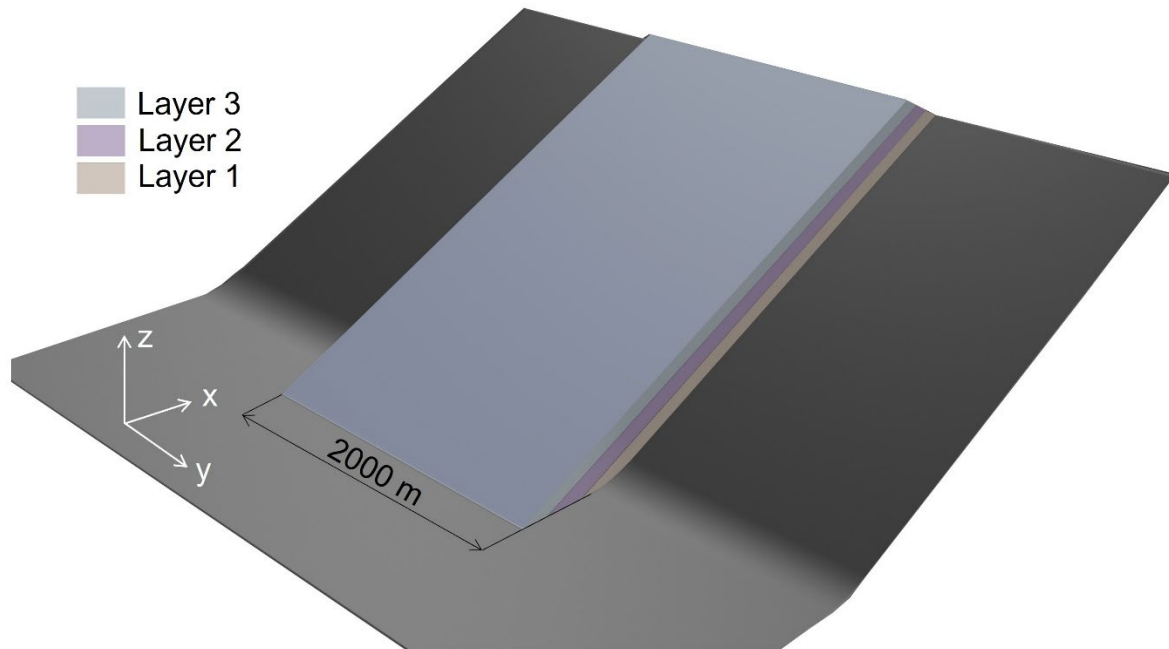
Along with the csv files, Python scripts are automatically generated to facilitate import to the 3D and VR visualization and animation tools Paraview and Blender 3, and to the game engine Unreal Engine 5. This workflow allows for the integration of r.avafLOW v4 simulation results with various levels of virtual reality.

### 3 Test cases and simulation design

#### 3.1 Generic planar rock slide with interlayer shearing

260 A computer-generated simplified landscape with an extent of 5000 x 5000 m is used for the demonstration of a planar rock slide, assuming the involvement of three discrete layers of rock. An inclined slope with a gradient of 0.5 runs out into a horizontal plane in down-slope (x) direction. The three planar sliding planes, with heights of 100 m each, forming the bases of the top, middle, and bottom layers, are aligned parallel to the main slope (Fig. 2).

Experiment SD1 uses the equilibrium-of-motion model, assuming an extremely slow movement. Model parameters are  
265 calibrated towards a plausible representation of layered sliding, where the motion along the sliding planes clearly dominates over the internal deformation of the individual layers. The settings are detailed in Table 3. All simulations are executed with densities of  $\rho = 2,700 \text{ kg m}^{-3}$ , and at a raster cell size of 10 m. The simulation is run for a process duration of 50,000 years, using a time scaling factor of  $31.536 \cdot 10^9$  ( $1 \text{ s} \rightarrow 1000 \text{ years}$ ).



270 **Fig. 2: Oblique view of the generic landscape with a three-layer release mass, used for the experiment SD1 on a planar rock slide. The main bodies of all layers are of equal thickness (100 m), and the surfaces of the two lower layers (not visible in this view) are arranged parallel to the surface of the upper layer.**

#### 3.2 Semi-generic Köfels rock slide

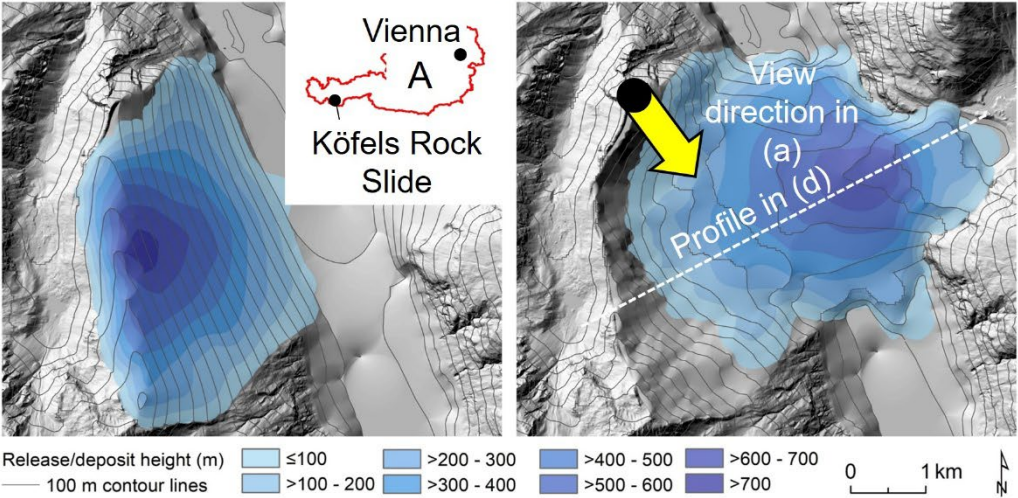
The Köfels rock slide has been thoroughly examined for more than a century (cf. Mergili and Prager, 2022 and references  
275 therein). The most recent reconstruction by Zangerl et al. (2021) builds the foundation for this case study. According to  $^{14}\text{C}$ -dating the event occurred 9527–9498 years before present (Nicolussi et al., 2015). The process originated from a head scarp

at the western slope of the central Ötz Valley, Austria, where the steep terrain exhibits a dip angle of 40 to 80°. The centre of the mass was displaced 2.6 km downslope (Sørensen and Bauer, 2003). Erismann et al. (1977) suggested a movement velocity of 50 m s<sup>-1</sup>.

(a) Oblique view of the Köfels rock slide from NW



(b) Reconstructed release height (c) Reconstructed deposit



(d) Longitudinal profile

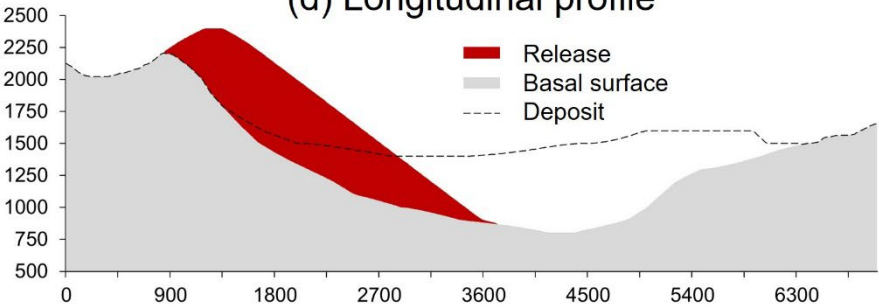


**Fig. 3: The prehistoric Köfels rock slide. (a) Oblique view from NW direction – author: M. Mergili, 3 August 2015; (b) and (c) reconstructed release and deposition masses – modified after Zangerl et al. (2021); (d) longitudinal profile through the rock slide area from SW to NE.**

285 The moved volume amounts to 3–4 km<sup>3</sup> and rock mass fragmentation and fracturing induced an increase by a factor of 1.26 (Zangerl et al., 2021). The sliding rock mass reached the entrance of the tributary Horlach Valley on the opposite side of the slope, where massive bedrock forced a halt. Up to the present day, the deposit is blocking the main valley. The sliding rock mass possibly split up, as proposed by Erismann and Abele (2001): the lower part might have stopped and deposited after the collision with the opposite slope, whereas the upper part moved one kilometre farther. Preuss (1986) reported about some evidence of a potential internal shear zone. This finding, however, has not yet been supported by field evidence. An alternative more likely scenario is the emergence of several internal shear zones facilitating the adaption to the terrain surface over the course of the substantial deformation of the rock mass. The rock slide deposit is extremely heterogenous, with characteristics ranging from completely disintegrated and crushed material to almost solid fractured rock. The pronounced vertical and horizontal variability in the degree of cataclasis and fracturing indicates complex internal deformation phenomena during the rock slide.

295 We consider this case study semi-generic, as there are considerable uncertainties regarding the pre-event topography and the characteristics of the rock slide and its internal deformation. Three computational experiments are performed (Table 3), using the standard flow model of r.avaflow (experiment KF1), the one-layer model with deformation control (KF2), and the multi-layer model with two layers and deformation control (KF3). For the multi-layer model, we assume a release mass composed of two layers of equal height distribution. All simulations only consider the released rock mass whereas, for simplicity, possibly entrained valley fill is neglected. The model parameters are optimized against the observed travel distance and deposit using an iterative trial-and-error procedure. Thereby, a time dependency of the deformation control and the fraction of global sliding is considered, in order to account for effects of increasing crushing and loss of coherence, related to the dynamic stresses the sliding mass is exposed to. All simulations are run with a density of  $\rho = 2,700 \text{ kg m}^{-3}$  and at a raster cell size of 15 m, considering a process duration of 120 s.

### 3.3 Semi-generic East Fogo landslide and tsunami

Fogo is an active volcanic island, that forms part of the Cape Verde archipelago in the Atlantic Ocean off the coast of Senegal, West Africa. Its highest peak is the stratovolcano Pico do Fogo (2829 m asl.), which sits at the bottom of a cauldron, bordered by a semi-circular, up to 1000 m high escarpment on the western, south-western, and north-western sides, and merging with the outer slope of the island on the eastern side (Fig. 4a). Various studies have investigated the volcanic and geomorphological history of the island, and there is broad agreement upon the fact that the cauldron was formed by giant landsliding, probably in various stages, and today's Pico do Fogo formed afterwards (e.g., Day et al., 1999; Marques et al., 2019; Barrett et al., 2020; Cornu et al., 2021). This has led to considerations of future risk. Possible tsunami deposits were



found on the neighbouring island of Santiago, but their real origin is disputed, and so are the number and total volume of  
 315 landslides, ranging from 20–300 km<sup>3</sup>, depending on the interpretation of the available evidence and the way of  
 reconstructing the pre-event terrain.

The aim of the present work is not to reconstruct the landsliding – often referred to as the East Fogo volcanic flank  
 collapse(s) – in all detail, but we use this case to demonstrate the effects of layering and controlled deformation for a very  
 large phenomenon. Our terrain reconstruction builds on the hypothesis of the existence of a former volcanic summit, named  
 320 Monte Amarelo (Cornu et al., 2021), which collapsed in one single event, and the sliding surface reaching down to the basis  
 of the volcanic edifice in the deep sea (worst-case assumption). Though our reconstruction is based on the available  
 topographic evidence, using the SRTM V4 (Jarvis et al., 2008) and the GEBCO\_2021 Grid (GEBCO Compilation Group,  
 2021) digital terrain models, it largely relies on the subjective reconstruction of the former terrain surface and the basal  
 sliding surface. As a result, we characterize the outcome as a semi-generic data set (Fig. 4b and 4c). The derived collapse  
 325 volume would be approx. 250 km<sup>3</sup>, which comes close to the maximum estimate of Day et al. (1999) (300 km<sup>3</sup>) and is much  
 higher than more recent estimates of maximum 160 km<sup>2</sup> (Martínez-Moreno et al., 2018).

Three computational experiments are applied to the semi-generic East Fogo event (FO1–FO3). They are computed at a raster  
 cell size of 270 m cell size and for a duration of 900 s. The key parameters for each of the experiments are summarized in  
 Table 3. For comparison, all simulations are repeated with the landslide material only, neglecting the ocean water.

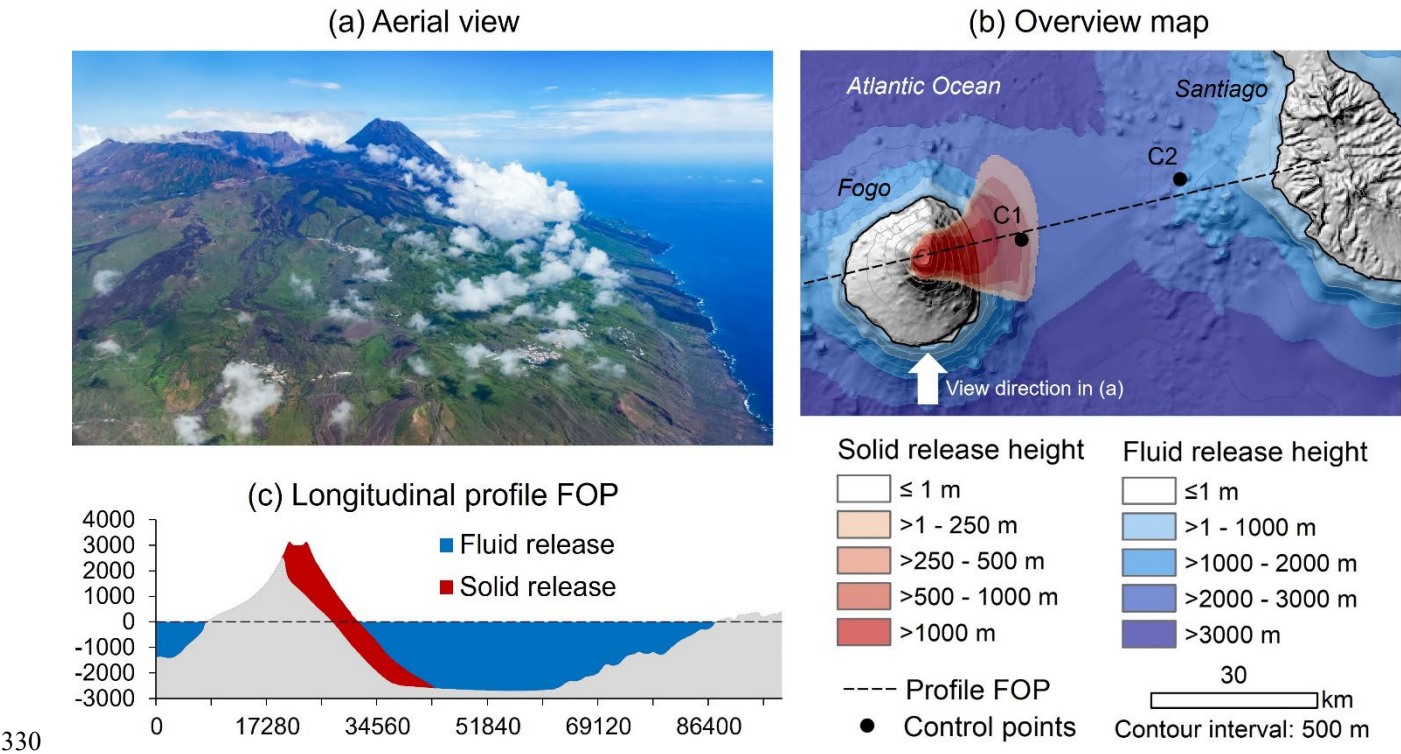


**Fig. 4: Prehistoric East Fogo event. (a) Aerial view of today’s situation with Pico do Fogo – author: M. Mergili, 10 September 2022; (b) Overview map with reconstructed release height distribution; (c) profile along the dashed line in (b).**

### 3.4 Semi-generic Dösen rock glacier

Since the 1990s, the Dösen rock glacier has been an important site for interdisciplinary permafrost and periglacial research in the eastern Austrian Alps (Kellerer-Pirklbauer et al., 2018). Located at the valley head, this rock glacier extends over roughly 1 km in length with a maximum width of approx. 340 m, resulting in an area of some 0.2 km<sup>2</sup> (Fig. 5). The landform covers a span of about 300 m in elevation (terminus at approx. 2500 m) with a mean slope angle of 24° (Wagner et al., 2020). The Dösen rock glacier is talus-derived and tongue-shaped with distinct longitudinal and transverse furrows and ridges and a steep front of up to 40 m in height (Kellerer-Pirklbauer et al., 2022). A 10 to 40 m thick permafrost body exists below an active layer of several metres. The geomorphic setting and results of Schmidt-hammer exposure-age dating suggest that rock glacier formation started after the retreat of the Younger Dryas glaciation and sometimes before 8400 years before present (Kellerer-Pirklbauer et al., 2018). Long-term records of pluriannual (1954 to 1995) and interannual (1995 until 2024) movement rates are complemented with climate and ground climate datasets (Kaufmann et al. 2007, Kellerer-Pirklbauer & Kaufmann, 2012; Kaufmann et al., 2016). For the period between 1995 and 2022, starting with the establishment of annual geodetic surveys, these records amount to a mean annual displacement rate of roughly 35 centimetres per year.

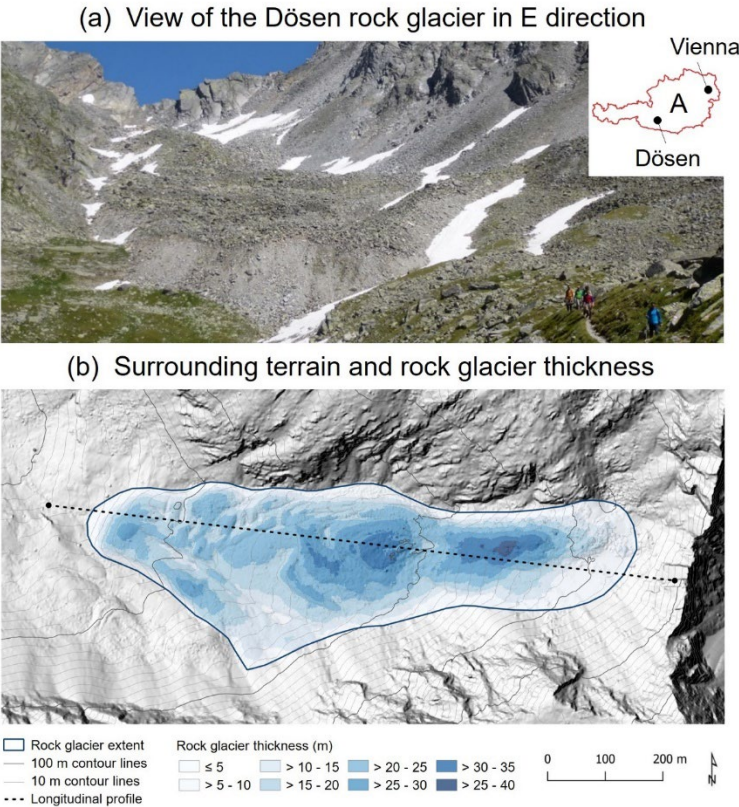


**Fig. 5: Dösen rock glacier. (a) Location of the rock glacier in Austria and view from the front towards the rooting zone – author: G. K. Lieb; (b) Rock glacier extent and simulation release height, to be understood as the reconstructed thickness of the rock glacier body, based on geophysical evidence and extrapolation (Kellerer-Pirklbauer et al., 2018).**

350 The computational experiment DO1 is applied to a simplified (therefore referred to as semi-generic) representation of the Dösen rock glacier (Fig. 5), using the slow-flow model. The simulation is executed at a raster cell size of 1 m for a duration of 300 years. Table 3 discloses the key parameters, which were calibrated in to reach plausible velocities and movement patterns, related to the measurements. Visualization is performed with and without draping of the dynamically adapted orthophoto, in order to additionally analyse the visual effects of the draping.

355

**Table 3: Summary of the key parameter settings applied to the simulations on the generic slope deformation (SD1), the prehistoric Köfels rock slide (KF1–KF3), the prehistoric East Fogo event (FO1–FO3), and the semi-generic Dösen rock glacier (DO1). L = layered model.**

Experiment		<i>Phase</i>	$\rho$	$\varphi, \delta$	$\nu$	$\zeta$	$f_d^*$	$f_g$	L
SD1	Extremely slow deformation	P1	2700		$10^{20}$	$5 \cdot 10^9$		1.0	Yes
		P2	2700		$10^{20}$	$2 \cdot 10^9$		1.0	
		P3	2700		$10^{20}$	$10^9$		1.0	
KF1	Standard model		2700	35, 10					No
KF2	One-layer model with deformation control		2700	35, 10			0.3–0.8	1.0–0.25	No
KF3	Two-layer model with deformation control	P1	2700	35, 12			0.2–0.6	1.0–0.0	Yes
		P3	2700	35, 11			0.2–0.8	0.8–0.0	
FO1	Standard model	P1	2700	35, 7			1.0	0.0	No
		P3	1000	0, 0				0.0	
FO2	Layered model	P1	2700	35, 7			1.0	0.0	Yes
		P3	1000	0, 0				0.0	
FO3	Layered model with deformation control	P1	2700	35, 7			0.0–0.8	1.0–0.0	Yes
		P3	1000	0, 0			1.0	0.0	
DO1	Extremely slow deformation		1800		$10^{11}$	$\infty$		0.0	No

## 4 Results

### 360 4.1 Generic planar rock slide with interlayer shearing

The equilibrium-of-motion model provides the expected results for the generic planar rock slide, including the formation of back-scarps characteristic for this type of process (Fig. 6). We note that the simulation outcomes are very sensitive to the



parameterization, with plausibility strongly depending on the balance between time scaling, internal viscosity, and basal viscosity in the equilibrium-of-motion model. Preliminary tests have shown that the result also strongly depends on the raster  
365 cell size applied to the simulation. With coarser cell size, numerical diffusion strongly blurs the layer heads, leading to a smoother deformation pattern.

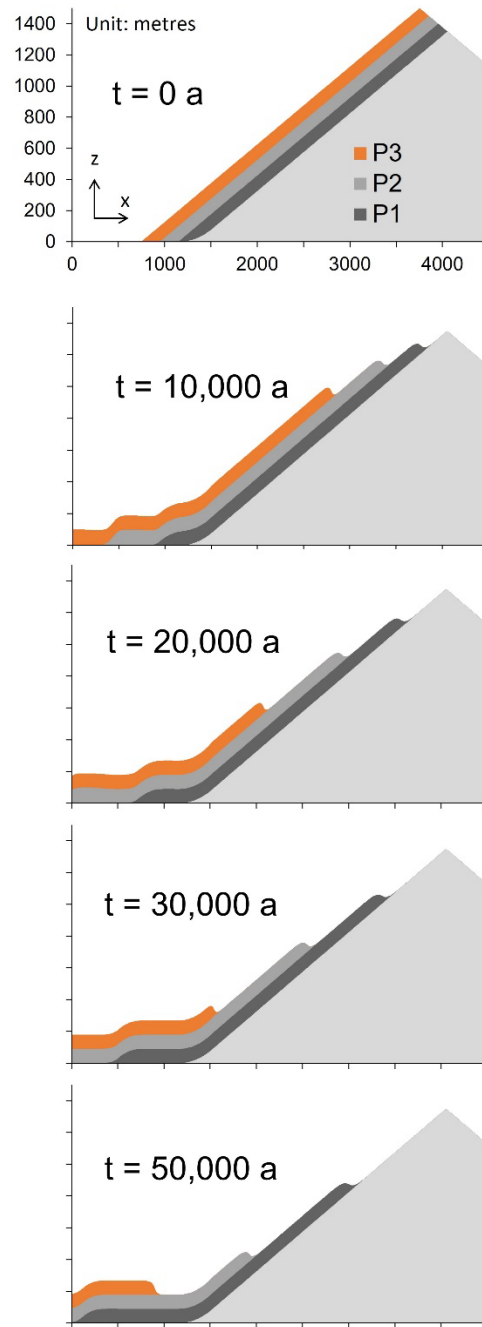


**Fig. 6: Flow height evolution for the experiment SD1 along a longitudinal profile in down-slope (x) direction, assuming an extremely slow movement.**

Fig. 7 and Fig. 8 illustrate the differences between the standard r.avaflow model (with one solid phase and full deformation), the one-layer model with controlled deformation, and the two-layer model with controlled deformation. The lower density and therefore larger volume and height of the heavily fractured to crushed rock mass, compared to the release mass, is considered in Fig. 7 and Fig. 8: simulated heights are multiplied with a factor up to 1.26, following Zangerl et al. (2021), since the models used in r.avaflow assume a constant density of the material throughout the entire duration of the process.

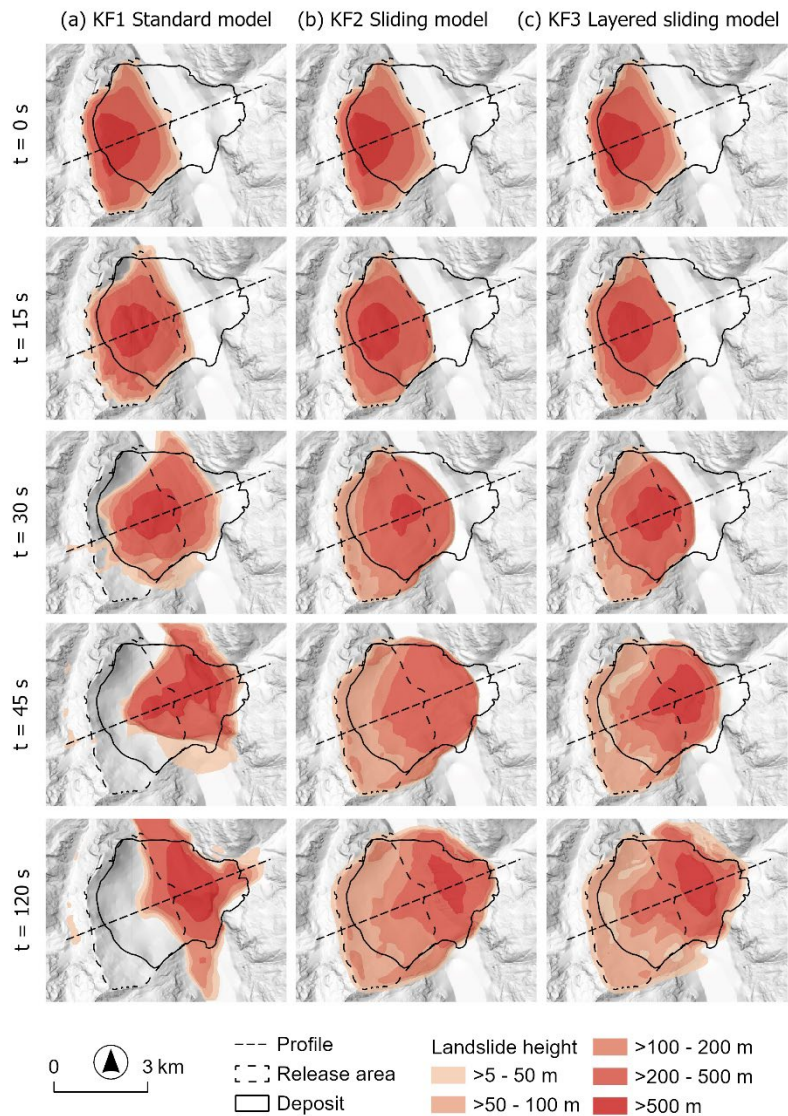


**Fig. 7: Evolution of flow height for the Köfels experiments KF1–KF3. (a) KF1: standard model without deformation control; (b) KF2: model with one layer, deformation control, and global sliding; (c) KF3: model with two layers, deformation control, and global sliding.**

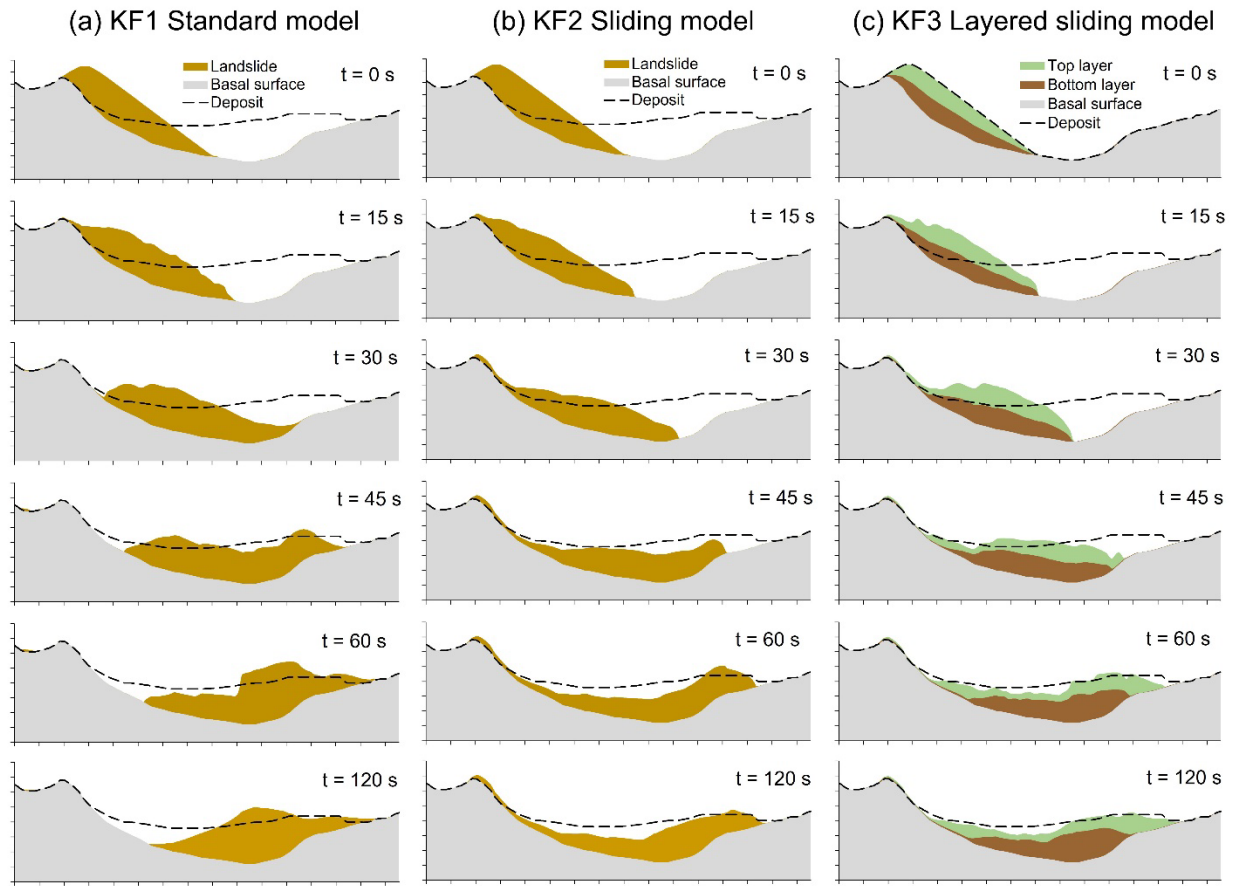


**Fig. 8: Flow height evolution for the Köfels experiments KF1–KF3 along the longitudinal profile depicted in Fig. 7. (a) KF1: standard model without deformation control; (b) KF2: sliding model with one layer (deformation control and global sliding); (c) KF3: sliding model with two layers (deformation control and global sliding).**

With the standard r.avaflow model (experiment KF1), the moving mass displays a strong extension in lateral direction, flowing up and down the Ötz Valley – a behaviour not corresponding to the shape of the observed deposit. This overestimate of lateral spreading is the expected behaviour for a flow model and therefore underlines the call for an approach more adequately representing sliding behaviour. The one-layer model with deformation control (experiment KF2) provides a more realistic representation of the rock slide evolution and deposition. The extent of lateral spreading up and down the Ötz Valley is strongly reduced while the travel distance in sliding direction is in correspondence with the observation (calibrated). Control of deformation, however, is applied at the cost of a reduced flexibility of the rock mass to adapt to the funnel shape at the outlet of Horlach Valley, so that the front of the simulated rock slide deposit is too wide: the reconstructed impact area is exceeded particularly at the N side (Fig. 7b). Also, the profiles in Fig. 8 reveal that the deposition height is underestimated in the proximal part of the deposition area and overestimated in the distal part. The two-layer model with controlled deformation (experiment KF3) has a strong generic component, as the splitting of the release mass into a top and a bottom

395 layer of equal height is considered due to a lack of more detailed information (Section 3.2; Zangerl et al., 2021). The main advantage of the siding surface between the two layers is that the lower layer can entirely deposit in the Ötz valley, whereas the upper layer can slide into the Horlach Valley, to correspond with the observed travel distance of the rock slide. This reduces the need to allow for a very strong deformation of the mass, resulting in a slightly more balanced distribution of the deposit along the flow path, compared to KF2 (Fig. 7 and Fig. 8).

400 In all simulations, process velocities and durations are plausible – considering the displacement of the centre of mass of 2.6 km and a velocity of  $50 \text{ m s}^{-1}$  (Erismann et al., 1977), we arrive at a process time of 52 s. Assuming acceleration and deceleration phases, this is in line with the observation that, in all experiments, the mass has almost reached its final position (corresponding to the position at  $t = 120 \text{ s}$  in Fig. 7 and Fig. 8) after 60 s.

### 4.3 Semi-generic East Fogo landslide and tsunami

405 The evolution of the displacement wave triggered by the semi-generic East Fogo volcanic flank collapse is illustrated in Fig. 9, Fig. 10, and Fig. 11, with the standard model and the layered model. Without layering (simulation FO1), the deposition area of the collapsed solid material remains a massive depression until the end of the simulation at  $t = 900 \text{ s}$ . Whilst it is expected that the displacement wave triggered by the impact of the collapse would create such a depression initially, it should be assumed that the restitution of the original sea surface starts soon thereafter – a behaviour which is, however, not reflected in the simulation results. Fig. 11 also displays this effect very clearly for the simulation FO1, showing a decrease of the sea level by maximum approx. 980 m for point C1 (Fig. 4), not recovering beyond a level of -900 m until the end of the simulation. A much more realistic behaviour of the system is achieved when applying the layered model (simulation FO2): after an initial positive anomaly caused by the passing of the solid material, the sea level drops to approx. -850 m at the point C1 at about the same time when the minimum is approached in FO1. However, immediately afterwards, the sea level starts to recover, even though some secondary and tertiary waves prevent it from exactly reaching its original state until the end of the simulation. In general, the displacement wave has a much lower magnitude in the simulation FO2 than in the simulation FO1. This phenomenon is most probably related to the different drag concepts used for the standard and layered models and requires some further discussion (Section 5.1). An interesting insight is provided by considering the same landslide with the assumption of a dry ocean basin (Fig. 9a and b). Under such dry conditions there is, as expected, no difference between the simulation results with the standard model and the layered model. When including the ocean water, the landslide becomes less mobile with both the standard model (FO1) and, to a much lesser extent, also with the layered model (FO2), due to the decelerating effect of the drag.

Fig. 9c depicts the flow heights for selected time steps as derived with the assumption of a slide-type movement (FO3), applied together with the layered model, whereas the flow height evolution at the points C1 and C2 (Fig. 4b) is illustrated in Fig. 11. There is less compression of the landslide along the down-slope direction with the sliding model, compared to the other simulations. In the flow models of FO1 and FO2, the internal deformation of the mass is prescribed by its geometry and by topography (Section 3.2; Pudasaini and Mergili, 2024a). With the controlled deformation employed in FO3, the mass

remains more stretched, mainly because the application of the global gravity components increases acceleration and decreases deceleration in the less steep frontal part, whereas the reverse is the case at the steeper tail. The magnitude of the displacement wave is smaller with FO3, compared to FO2. This phenomenon is most likely a consequence of the higher and steeper front of the flow-type landslide of simulation FO2: both the drag coefficient, as applied in the layered model, and the affected fraction of the water column are comparatively smaller in the case of the slide-type movement of simulation FO3 (Figure 1b).

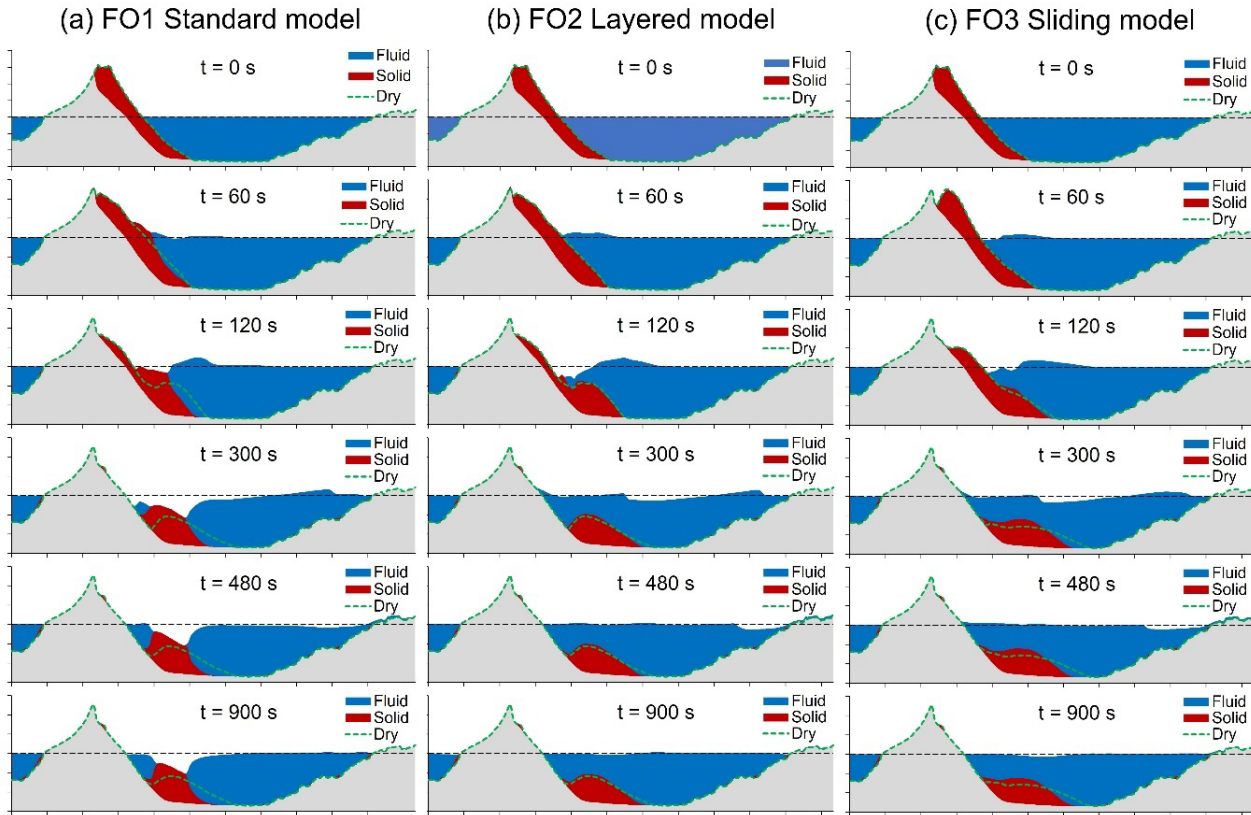


**Fig. 9: Prehistoric East Fogo event, effects of layering and deformation control on the evolution of flow height until  $t = 900$  s. Sections along profile FOP (Fig. 4b) for the simulations (a) FO1 (standard model); (b) FO2 (layered model); and (c) FO3 (model with deformation control). Note that the landslide deposit neglecting the interaction with the ocean is included in all profiles, referred to as “Dry”.**

#### 4.4 Semi-generic Dösen rock glacier

The simulation on the Dösen rock glacier provides plausible results, with a roughly continuous movement of few decimetres per year (Kaufmann et al. 2007, Kellerer-Pirklbauer & Kaufmann 2012; Kaufmann et al., 2016). Fig. 12 summarizes the main patterns obtained with the experiment DO1. Fig. 12b and Fig. 12c clearly reveal the substantial smoothing effect during the simulation, which are most likely associated with the TVD-NOC numerical scheme applied in r.avafLOW (Tai et al., 2002;



Wang et al., 2004). This means that the simulation can potentially reproduce or predict the motion of the rock glacier as a whole, whereas the fine-scale movement patterns are lost or at least blurred. In particular, the smaller geomorphological features typical of rock glaciers, such as ridges and furrows, are lost during the 300-year modelling period. For visualization purposes, particularly in the field of science-to-public communication, such fine-scale patterns, representing the morphological characteristics of rock glaciers, are essential to convey rock glacier dynamics and its geomorphic implication. This can be achieved by draping the distorted orthophoto over the rock glacier – fine-scale patterns are preserved in this way, and motion looks much more realistic than with the draped shaded relief map (Fig. 12d).

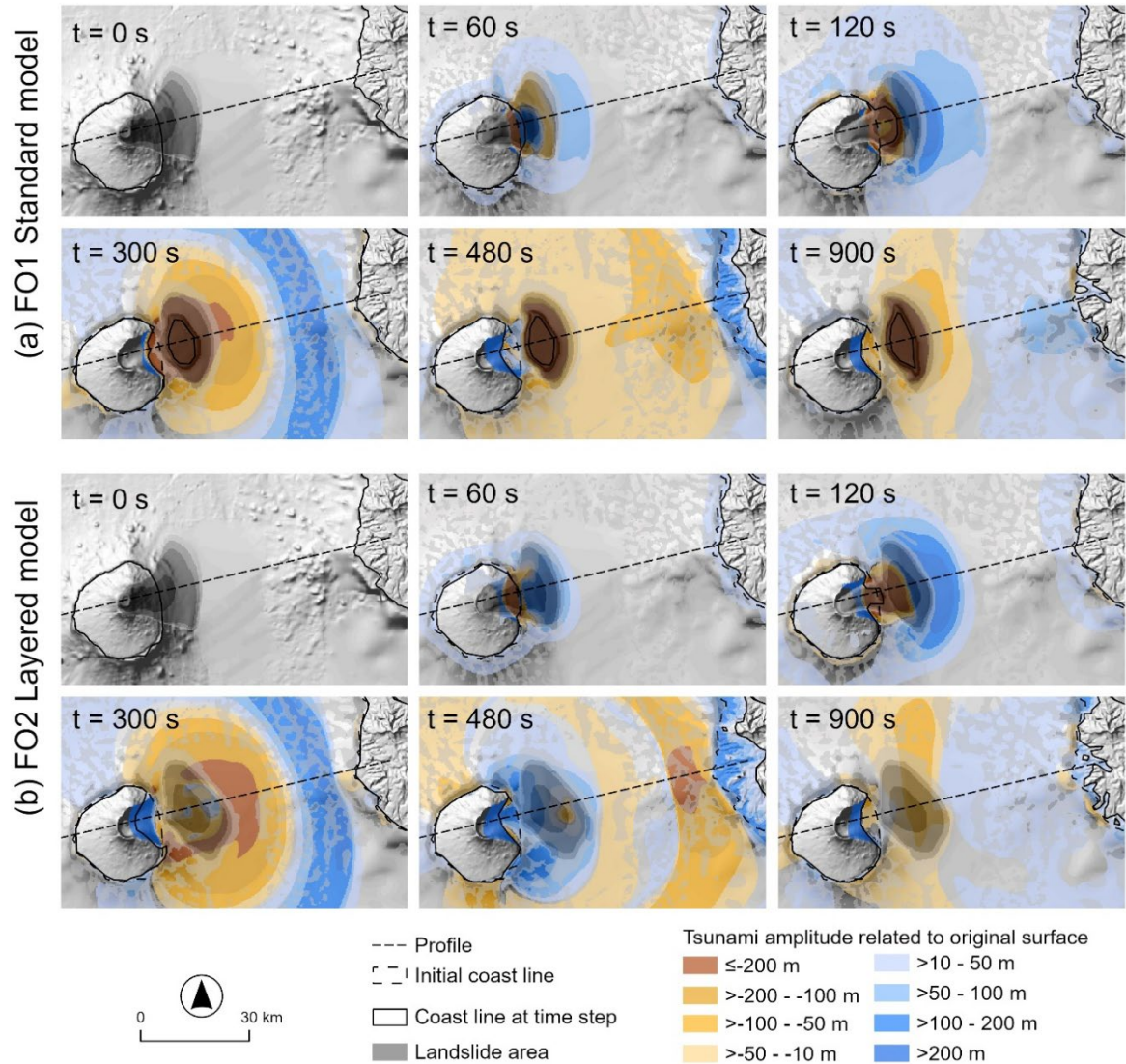
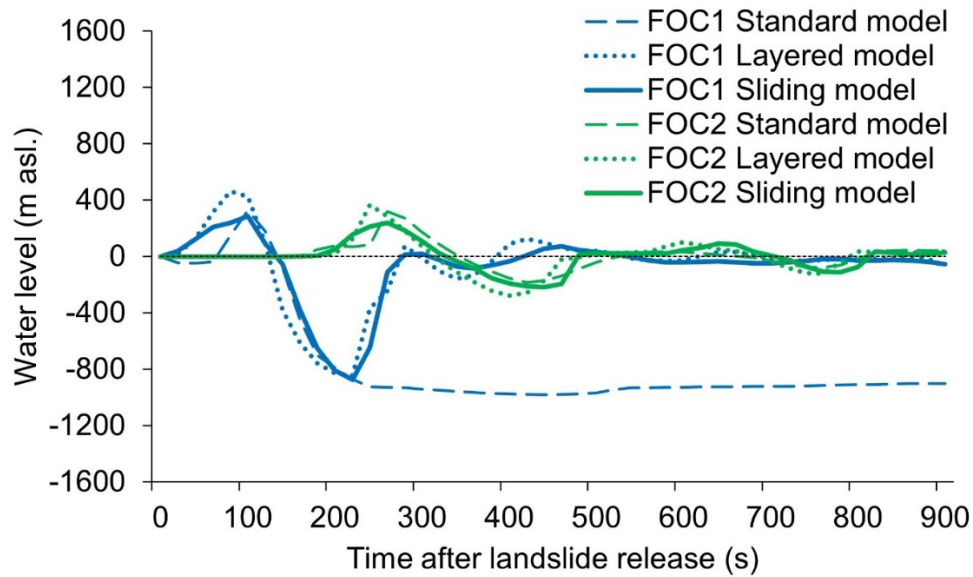
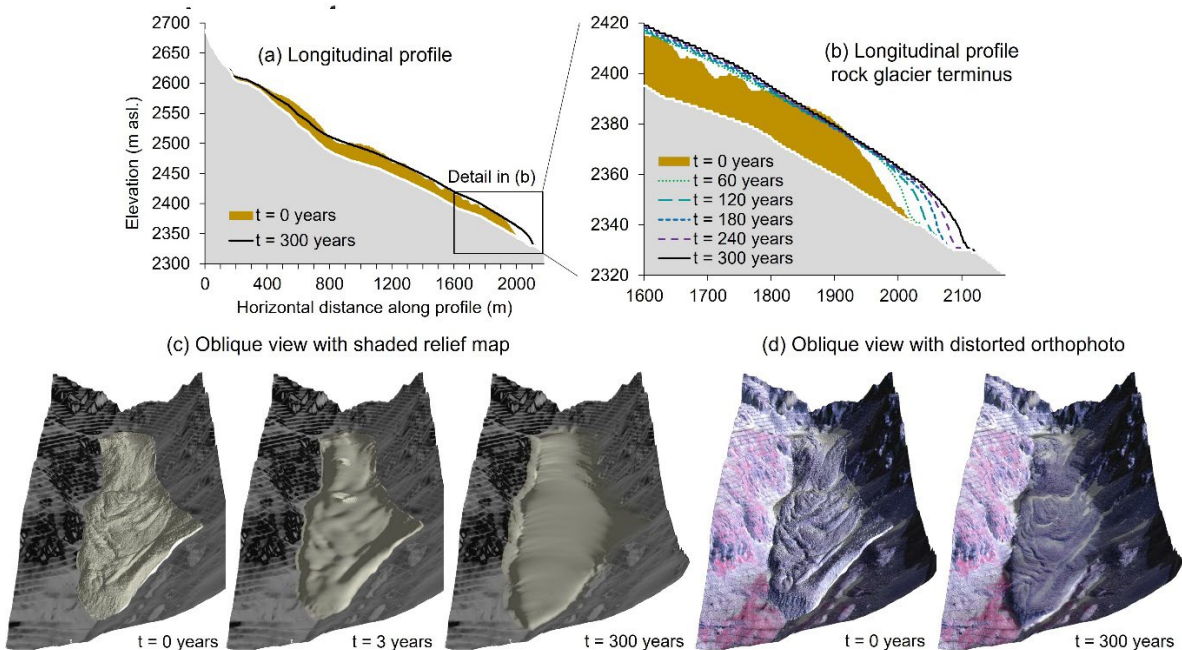


**Fig. 10: Prehistoric East Fogo event, effects of layering on the evolution of flow height until  $t = 900$  s. Map plots for (a) FO1 and (b) FO2 for selected time steps.**



455 **Fig. 11: Prehistoric East Fogo event, evolution of the sea surface (m asl.) at the control points C1 and C2 (Fig. 4b) until  $t = 900$  s for the simulations (a) FO1 (standard model), (b) FO2 (layered model), and (c) FO3 (sliding model).**



460 **Fig. 12: Simulation results for the semi-generic Dösen rock glacier case. (a) Longitudinal profile along the main flow line for  $t = 0$  and  $t = 300$  years including the rock glacier layer based on geophysical data. (b) Longitudinal profile, detail of the rock glacier terminus for six selected time steps. (c) Oblique view against the flow direction, shaded relief map for  $t = 0$ ,  $t = 3$  years, and  $t = 300$  years. (d) Oblique view with distorted orthophoto for  $t = 0$  and  $t = 300$  years.**



## 5 Discussion

r.avaflow v4 strongly builds on earlier versions of r.avaflow (first introduced by Mergili et al., 2017), but includes some important enhancements presented in the previous sections. We now discuss the potentials and limitations of these enhancements.

Sliding components have already been included in mass flow models by other authors, such as Bout et al. (2022) who used quite a complex approach, or Cicoira et al. (2022) who employed a computationally expensive full 3D model. To avoid the introduction of a large number of additional, often unknown, parameters and the need for high-performance computers, we decided to introduce a comparatively simple and straightforward approach, based on a mechanical deformation control (Pudasaini and Mergili, 2024a) and on the global gravity components. Fig. 6–Fig. 8 reveal that the model with deformation control introduced in Section 2 can be used to produce empirically fairly adequate representations of the prehistoric Köfels rock slide, and plausible results for the generic slope deformation outlined in section 4.1. This indicates that this model might be appropriate for the simulation of slide-type movements. However, it involves some physical, mathematical, and geometric/topographic simplifications, calling for an in-depth discussion of their scope of application and potentials for enhancement and improvement. First, this discussion picks up the complexity versus simplicity discourse regarding landslide modelling, following the hypothesis that simple models with fewer parameters can be preferable for practical application, compared to complex models with many parameters which are often unknown or, even if measurable, have to be calibrated to bring the models in line with the observations. In this sense, the deformation coefficient (Pudasaini and Mergili, 2024a), the fraction of global sliding, or the basal viscosity parameter can be considered either as mechanical or as empirical parameters with some physical background – a description which would, however, also be appropriate for established material parameters such as basal and internal friction, or viscosity. In contrast to established parameters, where a large pool of experiences can be used to choose plausible starting values for parameter optimization procedures and where, with other software packages, even well-established guiding parameter sets are available, the newly introduced values have to be calibrated from scratch. The deformation coefficient and the fraction of global sliding are intuitive quantities, strongly related to obvious characteristics of landslides. However, the time evolution of the model parameters, which can currently be prescribed based on “hard” time steps, relies on prior knowledge of the event. Coupling parameter evolution to dynamic flow characteristics such as velocity gradients could be an interesting future direction, increasing the physical meaning of the model.

The possibility to divide the sliding mass into multiple layers, and therefore to define horizons of shearing, increases the flexibility of the model with deformation control. Layering, however, is also important in another context: the simulations on the semi-generic East Fogo event clearly reveal that the standard r.avaflow model is not suitable for those simulations of landslide-to-reservoir impacts where a large landslide body comes to rest at the seafloor without substantial mixing with the water body. The explicit consideration of a layered movement (solid beneath fluid) is appropriate to realistically simulate the restitution of the original water surface (Fig. 9–Fig. 11). Technically, layering can be implemented in a relatively

straightforward way, largely by the adaptation of the gravity components and pressure gradients. A major difference between the standard model and the layered model is the drag. The concept of drag applied by Pudasaini and Mergili (2019) has been developed for mixtures of solid particles and fluid material, but not for layered landslides. The drag concept for layered movements, introduced in Section 2.3, represents a rough approximation which is supposed to work best in areas of spatially constant gradients of landslide thickness. Therefore, a direct comparison of the results of the corresponding simulations remains problematic. More research is required in this respect.

The slow-flow model proved to be useful in plausibly reproducing two fundamentally different processes, a three-layer planar rock slide (Fig. 6) and a rock glacier moving downvalley (Fig. 12). A detailed analysis on the correspondence of the empirically optimized viscosity parameters and parameters measured in comparable real-world cases are out of scope here, but the computational experiments reveal an important general limitation of *r.avaflow*, related to the TVD-NOC numerical scheme: fine-scale geomorphological patterns such as furrows and ridges are smoothed and blurred. For the Dösen rock glacier, we have shown an approach to visually compensate for this issue by distorting the orthophoto, following the direction of motion. A similar approach was demonstrated for the Köfels rock slide, to allow for a more realistic visual impression (cf. Supplementary materials). A solution to the blurring issue would have to rely on the implementation of a different numerical scheme, which should be a major direction for the future.

Another notable limitation regarding the simulation of large landslides is the application of depth-averaged models, where the height of the landslide should be much lower than the landslide length, and also much lower than the terrain curvature radius. For phenomena such as the Köfels rock slide or the East Fogo event, this condition might be violated, compromising the accuracy of the results. An in-depth benchmark comparison with full 3D models (e.g., Cicoira et al., 2022) would be helpful to learn about the magnitude of those effects. Until more benchmark tests and empirical evaluation efforts will be available, the proposed models should be used with utmost care when it comes to inform hazard zoning, technical protection measures, evacuation strategies, or other measures of “hard” risk management. The models are, however, useful for those purposes where a plausible representation of processes, achieved within short computational times and at high computational efficiency, is more important than high levels of mathematical, physical, and geometric accuracy.

Through the interfaces of *r.avaflow* v4 with the 3D visualization and animation software packages Paraview and Blender 3, and with the game engine Unreal Engine 5, simulation results can be converted into ordinary 3D videos, anaglyph videos, or immersive virtual reality experiences in a straightforward way. Such visually realistic representation of one- or multi-layer slide-type movements over a broad range of time scales and velocities without major computational efforts will be important to feed “gamification” (Pfeffer and Mergili, 2024) to create awareness and interest towards landslide phenomena within a broader audience at schools, museums, nature parks, universities, and other relevant social environments.

525 **6 Conclusions**

We have equipped the mass flow simulation tool *r.avaflow* with several additional functions to simulate (i) slide-type landslides with controlled deformation, (ii) layered landslides, and (iii) mass movements which are not extremely rapid. All these enhancements, included in *r.avaflow* v4, can be combined for the simulation of single- and multi-layer flow- and slide-type movements which can be extremely rapid to extremely slow. The model with deformation control builds on a small set of empirical parameters with a physical basis and yields plausible results for the test cases of the prehistoric K fels rock slide and a generic three-layer planar rock slide. For landslide-reservoir interactions, when the mixing between the landslide material and the water body is insignificant, the consideration of a layered movement results in a much more realistic restitution of the pre-event water level after alleviation of the primary displacement wave, compared to the standard multi-phase model used in *r.avaflow* that assumes phase mixing. Direct comparison between the standard model and the layered model remains a challenge due to different drag concepts to be applied. The slow-flow model proves capable of simulating even very slow movements such as a generic planar rock slide or a slowly downward moving rock glacier in a plausible way. Topographic details of modelled landforms (e.g., furrows and ridges of rock glaciers) are lost for numerical reasons but can be at least visually recreated through draping of a dynamically distorted orthophoto.

The enhanced flexibility of *r.avaflow* v4, compared to earlier versions of the software, increases the responsibility of the users to combine terms in a meaningful way. All the extensions introduced, and their interconnection, use simplifications and generalizations, which may lead to the loss of some physical details on the one hand, and a more straightforward parameterization on the other hand. Therefore, these models have to be exposed to additional benchmarking and empirical evaluation with well-documented real-world cases, in order to learn more about the effects of possible limitations of the new functionalities and to constrain suitable parameter values, to become ready for predictive applications in risk management. Furthermore, we plan to implement in a further tool-development step an intelligent warning function to inform users when they enter inappropriate combinations of parameter values. Until then, caution should be exercised when using the proposed models in “hard” risk management contexts, such as early warning systems and spatial planning. Nevertheless, the models represent an important resource for raising awareness and environmental education when used in combination with the newly implemented 3D animation and virtual reality interfaces of *r.avaflow* v4.

550 **Code availability**

*r.avaflow* 4.0G Revision 6, which was used for the simulations presented in Section 3 and Section 4, is provided in the Assets (Mergili, 2024; <https://doi.org/10.5281/zenodo.14005917>). The latest version of the code is available from Mergili and Pudasaini (2025). Please see Mergili and Pudasaini (2025) for software requirements and a detailed manual on how to run *r.avaflow* 4.0G.

## 555 **Data availability**

All the data and the start scripts required to run the simulations presented in Section 3 and Section 4 with r.avaflow 4.0G are provided in the Assets (Mergili, 2024; <https://doi.org/10.5281/zenodo.14005917>). Please consult Mergili and Pudasaini (2025) for software requirements and a detailed manual on how to run r.avaflow 4.0G. In addition, 3D animations of all the experiments SD1, KF1–KF3, FO1–FO3, and DO1 are provided in standard and anaglyph view. These animations were  
560 created directly from the simulation results with the software packages Blender 3 and Adobe Premiere Pro.

## **Author contributions**

Martin Mergili (MM), Hanna Pfeffer (HP), Andreas Kellerer-Pirklbauer (AKP), Christian Zangerl (CZ), Shiva P. Pudasaini (SP)

MM has contributed to the conceptualization and methodology of the research, designed the software, performed the formal  
565 analysis, visualization, validation, and most of the writing of the original draft. HP, AKP, and CZ have contributed to the data preparation and review and editing of the manuscript. SP has provided input in terms of methodology and review and editing of the manuscript.

## **Competing interests**

The authors declare that they have no conflict of interest.

## 570 **Acknowledgements**

This work is part of the project "Moving mountains - landslides as geosystem services in Austrian geoparks" (ESS22-24 - MOVEMONT) funded through the Earth System Sciences programme of the Austrian Academy of Sciences. Shiva P. Pudasaini acknowledges the financial support from the German Research Foundation (DFG) through the research project "Landslide mobility with erosion: Proof-of-concept and application—Part I: Modeling, Simulation and Validation" with the  
575 project number 522097187.

## **References**

Barrett, R., Lebas, E., Ramalho, R., Klaucke, I., Kutterolf, S., Klügel, A. et al. (2020): Revisiting the tsunamigenic volcanic flank collapse of Fogo Island in the Cape Verdes, offshore West Africa. Geological Society, London, Special Publications, 500, 13–26. <https://doi.org/10.1144/SP500-2019-187>

- 580 Cicoira, A., Blatny, L., Li, X., Trottet, B. & Gaume, J. (2022): Towards a predictive multi-phase model for alpine mass movements and process cascades. *Engineering Geology*, 310, 106866. <https://doi.org/10.1016/j.enggeo.2022.106866>
- Christen, M., Kowalski, J. & Bartelt, P. (2010): RAMMS: Numerical simulation of dense snow avalanches in three-dimensional terrain. *Cold Regions Science and Technology*, 63, 1–14. <https://doi.org/10.1016/j.coldregions.2010.04.005>
- Cornu, M.N., Paris, R., Doucelance, R., Bachélery, P., Bosq, C., Auclair, D. et al. (2021): Exploring the links between  
585 volcano flank collapse and the magmatic evolution of an ocean island volcano: Fogo, Cape Verde. *Scientific Reports*, 11, 17478. <https://doi.org/10.1038/s41598-021-95453-0>
- Day, S.J., Da Silva, S.H. & Fonseca, J.F.B.D. (1999): A past giant lateral collapse and present-day flank instability of Fogo, Cape Verde Islands. *Journal of Volcanology and Geothermal Research*, 94, 191–218. [https://doi.org/10.1016/S0377-0273\(99\)00103-8](https://doi.org/10.1016/S0377-0273(99)00103-8)
- 590 Erismann, T.H., Heuberger, H. & Preuss, E. (1977): Der Bimsstein von Köfels (Tirol), ein Bergsturz-“Friktionit”. *Tschermaks Mineralogische und Petrographische Mitteilungen*, 24, 67–119. <https://doi.org/10.1007/BF01083351>
- Erismann, T.H. & Abele, G. (2001): *Dynamics of rockslides and rockfalls*. Springer, Berlin. <https://doi.org/10.1007/978-3-662-04482-7>
- GEBCO Compilation Group (2021): GEBCO 2021 Grid. <https://doi.org/10.5285/c6612cbe-50b3-0cffe053-6c86abc09f8f>
- 595 GRASS Development Team (2025): Geographic Resources Analysis Support System (GRASS) Software. Open Source Geospatial Foundation. <https://grass.osgeo.org>
- Heim, A. (1932): Bergsturz und Menschenleben. *Geologische Nachlese* 30, Beiblatt zur Vierteljahresschrift der Naturforschenden Gesellschaft in Zürich, 20.
- Hungr, O., Leroueil, S. & Picarelli, L. (2014): The Varnes classification of landslide types, an update. *Landslides*, 11, 167–  
600 194. <https://doi.org/10.1007/s10346-013-0436-y>
- Jarvis, A., Guevara, E., Reuter, H.I. & Nelson, A.D. (2008): Hole-filled SRTM for the globe: version 4: data grid. CGIAR Consortium for Spatial Information. <https://srtm.csi.cgiar.org>
- Kellerer-Pirklbauer, A. & Kaufmann, V. (2012): About the relationship between rock glacier velocity and climate parameters in central Austria. *Austrian Journal of Earth Sciences*, 105 (2), 94–112.
- 605 Kellerer-Pirklbauer, A., Lieb, G. K., & Kaufmann, V. (2018): The Dösen Rock Glacier in Central Austria. A key site for multidisciplinary long-term rock glacier monitoring in the Eastern Alps. *Austrian Journal of Earth Sciences* 110 (2). <https://doi.org/10.17738/ajes.2017.0013>
- Kellerer-Pirklbauer, A., Lieb, G.K. & Kaufmann, V. (2022): Rock glaciers in the Austrian Alps: a general overview with a special focus on Dösen Rock Glacier, Hohe Tauern Range. In: Embleton-Hamann, C. (Ed.): *Landscapes and Landforms of Austria*, World Geomorphological Landscapes, Springer, Cham, 393–406. [https://doi.org/10.1007/978-3-030-92815-5\\_27](https://doi.org/10.1007/978-3-030-92815-5_27)
- 610 Marques, F.O., Hildenbrand, A., Victória, S.S., Cunha, C. & Dias, P. (2019): Caldera or flank collapse in the Fogo volcano? What age? Consequences for risk assessment in volcanic islands. *Journal of Volcanology and Geothermal Research*, 388, 106686. <https://doi.org/10.1016/j.jvolgeores.2019.106686>

- Martínez-Moreno, F.J., Santos, F.M., Madeira, J., Pous, J., Bernardo, I., Soares, A. et al. (2018): Investigating collapse structures in oceanic islands using magnetotelluric surveys: The case of Fogo Island in Cape Verde. *Journal of Volcanology and Geothermal Research*, 357, 152–162. <https://doi.org/10.1016/j.jvolgeores.2018.04.025>
- Mergili, M., Fischer, J.T., Krenn, J. & Pudasaini, S.P. (2017): r.avaflow v1, an advanced open-source computational framework for the propagation and interaction of two-phase mass flows. *Geoscientific Model Development*, 10, 553–569. <https://doi.org/10.5194/gmd-10-553-2017>
- Mergili, M., Emmer, A., Juřicová, A., Cochachin, A., Fischer, J.T., Huggel, C. & Pudasaini, S.P. (2018a): How well can we simulate complex hydro-geomorphic process chains? The 2012 multi-lake outburst flood in the Santa Cruz Valley (Cordillera Blanca, Perú). *Earth Surface Processes and Landforms*, 43, 1373–1389. <https://doi.org/10.1002/esp.4327>
- Mergili, M., Frank, B., Fischer, J.T., Huggel, C. & Pudasaini, S.P. (2018b): Computational experiments on the 1962 and 1970 landslide events at Huascarán (Peru) with r.avaflow: Lessons learned for predictive mass flow simulations. *Geomorphology*, 322, 15–28. <https://doi.org/10.1016/j.geomorph.2018.08.016>
- Mergili, M., Jaboyedoff, M., Pullarello, J. & Pudasaini, S.P. (2020a): Back calculation of the 2017 Piz Cengalo–Bondo landslide cascade with r.avaflow: what we can do and what we can learn. *Natural Hazards and Earth System Sciences*, 20, 505–520. <https://doi.org/10.5194/nhess-20-505-2020>
- Mergili, M., Pudasaini, S.P., Emmer, A., Fischer, J.T., Cochachin, A. & Frey, H. (2020b): Reconstruction of the 1941 GLOF process chain at lake Palcacocha (Cordillera Blanca, Peru). *Hydrology and Earth System Sciences*, 24, 93–114. <https://doi.org/10.5194/hess-24-93-2020>
- Mergili, M. & Prager, C. (2022): Giant “Bergsturz” landscapes in the Tyrol. In: Embleton-Hamann, C. (Ed.): *Landscapes and Landforms of Austria*, Springer, Cham, 311–325. [https://doi.org/10.1007/978-3-030-92815-5\\_22](https://doi.org/10.1007/978-3-030-92815-5_22)
- Mergili, M. (2024): r.avaflow v4, a multi-purpose landslide simulation framework – Simulation package for discussion paper. Zenodo. <https://doi.org/10.5281/zenodo.14005917>
- Mergili, M. & Pudasaini, S.P. (2025): r.avaflow – The mass flow simulation tool. <https://www.avaflow.org>
- Nicolussi, K., Spötl, C., Thurner, A. & Reimer, P.J. (2015): Precise radiocarbon dating of the giant Kőfels landslide (Eastern Alps, Austria). *Geomorphology*, 243, 87–91. <https://doi.org/10.1016/j.geomorph.2015.05.002>
- Pfeffer, H. & Mergili, M. (2024): Level Up Learning: A user-friendly game engine template for virtual reality landslide experiences (No. EGU24-1785). *Copernicus Meetings*. <https://doi.org/10.5194/egusphere-egu24-1785>
- Preuss, E. (1986): Gleitflächen und neue Friktionitfunde im Bergsturz von Kőfels im Ötztal, Tirol. *Material und Technik*, 3.
- Pudasaini, S.P. (2012): A general two-phase debris flow model. *Journal of Geophysical Research: Earth Surface*, 117, F03010. <https://doi.org/10.1029/2011JF002186>
- Pudasaini, S.P. & Mergili, M. (2019): A multi-phase mass flow model. *Journal of Geophysical Research: Earth Surface*, 124, 2920–2942. <https://doi.org/10.1029/2019JF005252>
- Pudasaini, S.P. (2023): Dispersive landslide. *International Journal of Non-Linear Mechanics*, 150, 104349. <https://doi.org/10.1016/j.ijnonlinmec.2023.104349>

- Pudasaini, S.P. & Mergili, M. (2024a): Mechanically controlled landslide deformation. *Journal of Geophysical Research: Earth Surface*, 129(5), e2023JF007466. <https://doi.org/10.1029/2023JF007466>
- 650 Pudasaini, S.P. & Mergili, M. (2024b): Landslide dynamics with energy loss in internal shearing. *Landslides*, 22, 1491–1507. <https://doi.org/10.1007/s10346-024-02424-4>
- Pudasaini, S.P., Mergili, M., Lin, Q. & Wang, Y. (2024): Dynamic simulation of rock-avalanche fragmentation. *Journal of Geophysical Research: Earth Surface*, 129(9), e2024JF007689. <https://doi.org/10.1029/2024JF007689>
- 655 Sattar, A., Cook, K., Rai, S.K., Berthier, E., Allen, S., Rinzin, S. et al. (2025): The Sikkim flood of October 2023: drivers, causes and impacts of a multi-hazard cascade. *Science*, 387, eads2659. <https://doi.org/10.1126/science.ads2659>
- Savage, S.B. & Hutter, K. (1989): The motion of a finite mass of granular material down a rough incline. *Journal of Fluid Mechanics*, 199, 177–215. <https://doi.org/10.1017/S0022112089000340>
- Shugar, D.H., Jacquemart, M., Shean, D., Bhushan, S., Upadhyay, K., Sattar, A. et al. (2021): A massive rock and ice avalanche caused the 2021 disaster at Chamoli, Indian Himalaya. *Science*, 373, 300–306.
- 660 <https://doi.org/10.1126/science.abh4455>
- Sørensen, S.A. & Bauer, B. (2003): On the dynamics of the Kőfels sturzstrom. *Geomorphology*, 54, 11–19. [https://doi.org/10.1016/S0169-555X\(02\)00349-7](https://doi.org/10.1016/S0169-555X(02)00349-7)
- Su, C., Mergili, M., Rana, N.M., Zhang, S., Dai, C., Wang, B. & Han, Y. (2024): Failure analysis and flow dynamic modeling using a new slow-flow functionality: the 2022 Jiaokou (China) tailings dam breach. *Landslides*, 21, 379–391.
- 665 <https://doi.org/10.1007/s10346-023-02158-2>
- Tai, Y.C., Noelle, S., Gray, J.M.N.T. & Hutter, K. (2002): Shock-capturing and front-tracking methods for granular avalanches. *Journal of Computational Physics*, 175, 269–301. <https://doi.org/10.1006/jcph.2001.6964>
- van Den Bout, B., Van Asch, T., Hu, W., Tang, C.X., Mavrouli, O., Jetten, V.G. & Van Westen, C.J. (2021): Towards a model for structured mass movements: the OpenLISEM hazard model 2.0 a. *Geoscientific Model Development*, 14, 1841–1864. <https://doi.org/10.5194/gmd-14-1841-2021>
- 670 van den Bout, B., Tang, C., van Westen, C. & Jetten, V. (2022): Physically based modeling of co-seismic landslide, debris flow, and flood cascade. *Natural Hazards and Earth System Sciences*, 22, 3183–3209. <https://doi.org/10.5194/nhess-22-3183-2022>
- Vilca, O., Mergili, M., Emmer, A., Frey, H. & Huggel, C. (2021): Reconstruction of the sudden drainage of a moraine-dammed lake in the Cordillera Vilcabamba (Peru): the 2020 Salkantay event. In *EGU General Assembly Conference Abstracts*, EGU21-13584. <https://doi.org/10.5194/egusphere-egu21-13584>
- Voellmy, A. (1955): Über die Zerstörungskraft von Lawinen. *Schweizerische Bauzeitung*, 73, 159–165.
- Wagner, T., Ribis, M., Kellerer-Pirklbauer, A., Krainer, K. & Winkler, G. (2020): The Austrian rock glacier inventory RGI\_1 and the related rock glacier catchment inventory RGCI\_1 in ArcGis (shapefile) format. *PANGAEA*.
- 680 <https://doi.org/10.1594/PANGAEA.921629>

- Wang, Y., Hutter, K. & Pudasaini, S.P. (2004): The Savage-Hutter theory: a system of partial differential equations for avalanche flows of snow, debris, and mud. *ZAMM–Journal of Applied Mathematics and Mechanics / Zeitschrift für Angewandte Mathematik und Mechanik*, 84, 507–527. <https://doi.org/10.1002/zamm.200410189>
- 685 Yildiz, A., Zhao, H. & Kowalski, J. (2023): Computationally-feasible uncertainty quantification in model-based landslide risk assessment. *Frontiers in Earth Science*, 10, 1032438. <https://doi.org/10.3389/feart.2022.1032438>
- Zangerl, C., Schneeberger, A., Steiner, G. & Mergili, M. (2021): Geographic-information-system-based topographic reconstruction and geomechanical modelling of the Kőfels rockslide. *Natural Hazards and Earth System Sciences*, 21, 2461–2483. <https://doi.org/10.5194/nhess-21-2461-2021>
- 690 Zheng, G., Mergili, M., Emmer, A., Allen, S., Bao, A., Guo, H. & Stoffel, M. (2021): The 2020 glacial lake outburst flood at Jinwucuo, Tibet: causes, impacts, and implications for hazard and risk assessment. *The Cryosphere Discussions*, 2021, 1–28. <https://doi.org/10.5194/tc-2021-335>